THE JOURNAL OF PHYSICAL CHEMISTRY C
A JOURNAL OF THE AMERICAN CHEMICAL SOCIETY

pubs.acs.org/JPCC
Article

Structural Features Governing the Near-Edge X-ray Absorption Spectra of Lead Halide Perovskites

Simone Virga, Alessandro Longo, Candida Pipitone, and Francesco Giannici*

Cite This: J. Phys. Chem. C 2023, 127, 18058−18066
Read Online

ACCESS | Metrics & More | Article Recommendations | Supporting Information

ABSTRACT: X-ray absorption spectroscopy (XAS) represents the ideal complement to diffraction techniques to investigate the structure of materials. Despite its strong points and the abundance of studies devoted to lead halide perovskites for application in optoelectronics, XAS has been applied to lead halide perovskites rather infrequently to date, and with varying degrees of success. In the search of generalizable approaches to be applied to data analysis of XAS spectra of halide perovskites with different compositions, we present here an experimental and computational study on a hybrid Pb/Bi iodide solid solution as a model for halide perovskites with different compositions.

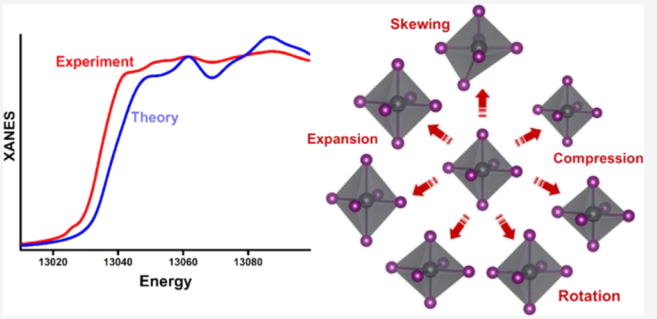

1. INTRODUCTION

Since their first use in 2009 as photosensitizers in solar cells,[1] hybrid lead halide perovskites have been at the forefront of materials chemistry research for almost two decades. Every aspect of composition, morphology, and processing of methylammonium lead iodide has been the subject of scrutiny and optimization, leading now to almost 30% efficiency in tandem solar cells.[2] However appealing, lead iodide perovskites suffer from two fundamental issues, namely, lead toxicity and limited stability to ambient conditions, stimulating in turn many lines of investigation in materials chemistry. In search of other p-block cations to substitute lead, and improved ambient stability, many different organic−inorganic hybrid metal halide compositions have been proposed recently.[3,4] They may often crystallize layered, monodimensional, or zero-dimensional structures, collectively referred to as perovskites, although they can display various kinds of octahedral connectivity often far from the perovskite arystotype.[5−7] Although materials research has mostly focused on low-bandgap compositions, wide-bandgap (>1.7 eV) halide perovskites have progressively emerged as possible candidates for several uses as well.[8,9]

$(TMSO)PbI_3$ and $(TMSO)_3Bi_2I_9$ (with TMSO = trimethylsulfoxonium, $(CH_3)_3SO^+$) form a solid solution with a monodimensional pseudo-perovskite structure with edge-sharing octahedra containing either Pb^{2+}, Bi^{3+}, or a metal cation vacancy, the latter being required to keep charge neutrality.[10] Their rich defect chemistry and ordering in metal cation sites have been recently described in detail.[11,12]

X-ray absorption near-edge structure (XANES), possibly with high-energy resolved fluorescence detection (HERFD-XANES), has been proven to be a powerful tool to assess the oxidation state, coordination geometry, and metal−ligand interactions in a wide range of natural and artificial materials, complementing conventional diffraction and electron microscopy techniques.[13−19] In general, near-edge spectra do not suffer from loss of resolution due to thermal or static disorder as much as the extended X-ray absorption fine structure (EXAFS), and their applicability is therefore much broader.

While XANES and HERFD-XANES are now well-established tools in the study of chalcogenides, in general, and almost routinely employed for, e.g., heterogeneous catalysis or metallobiology, their application to the booming field of halide perovskites has been very sparse to date. On the other hand, the effects of even subtle structural features, or the choice of calculation details such as spin-orbit coupling, on the predicted frontier electronic states and optical transitions have been extensively investigated in several detailed papers.[20,21] Only in the last few years, some studies have appeared, devoted specifically to the analysis of XANES spectra of halide perovskites and lower-dimensional pseudo-perovskites. In particular, Gardner and co-workers reported the HERFD-XANES and resonant inelastic X-ray scattering (RIXS) spectra of MAPI, $Cs_3Bi_2I_9$, $APbI_4$, APb_2I_6: a 3D perovskite, two 2D edge-sharing layered pseudo-perovskites, and a 1D face-sharing pseudo-perovskite, respectively.[22−24]

Smith et al. used in situ XANES to follow the oxidation of Sn(II) to Sn(IV) in formamidinium-based thin films.[25]

Received: May 29, 2023
Revised: August 22, 2023
Published: September 1, 2023

https://doi.org/10.1021/acs.jpcc.3c03604
J. Phys. Chem. C 2023, 127, 18058−18066

Vorwerk et al. used many-body perturbation theory to assess the excitonic binding energy of the core-holes at the low-energy I L_3-edge and Pb M_5-edge of MAPI, finding that the main features of these spectra are essentially determined by the inorganic Pb−I framework by comparison with PbI_2.[26]

Drisdell et al. strived instead for an ab initio modeling of the metal XANES spectra, constructing a statistical number of snapshots of the methylammonium lead iodide/bromide (MAPI/MAPBr) structure with ab initio molecular dynamics. In this thorough investigation, they concluded that I/Br are randomly distributed in MAPI/MAPBr solid solutions. In addition, they found that the spectra are highly sensitive to Pb-halide distances and octahedral tilting and especially that thermal motions dominate any possible structural conformation that could be preferred energetically.[27]

In the following, we present a comprehensive theoretical assessment of near-edge spectra of metal and iodide atoms alike in a 1D halide pseudo-perovskite. In search of generally applicable criteria, the ab initio simulations of the spectra and pDOS are carried out with a bottom-up approach, starting from the $[PbI_6]^{4-}$ and $[BiI_6]^{3-}$ octahedral units common to any (pseudo-)perovskite, up to the complete $(TMSO)_3(Pb,Bi)I_{9-x}$ structure. All possible patterns of Pb/Bi substitution in a supercell with eight metal sites to account for multiple scattering effects between neighboring metals have been also included. We then compare the simulations with experimental XANES spectra, highlighting that these can be effectively modeled with just $[PbI_6]^{4-}$ and $[BiI_6]^{3-}$ units but also carry indirect information about the long-range structure.

Core-level spectroscopy methods like XANES give fundamentally different chemical insights from valence-level techniques like photoelectron spectroscopy methods (UPS or XPS). The latter provides immediate information on empty states close to the band gap directly at the surface, so they can be conveniently complemented by the bulk average information only accessible to core-level spectroscopy methods.

2. METHODS

Samples with general formula $(TMSO)_3Pb_{3x}Bi_{2(1-x)}I_9$ were synthetized through precipitation from aqueous solution as described in detail in our earlier work.[10] All powders were decanted for 24 h and then filtered through 0.45 μm polypropylene filters (Millipore).

X-ray diffraction patterns were acquired on all samples with a Rigaku Miniflex 600 diffractometer using Ni-filtered Cu Kα radiation and analyzed with Rietveld refinement using GSAS-II.[28] All samples were refined with an orthorhombic *Pnma* structure. Accurate stoichiometry was derived using established relations between lattice parameter ***a*** and compositions[10] (details reported in the SI).

X-ray absorption spectra were acquired at the Pb and Bi L_3-edge at the XAFS beamline of Elettra Sincrotrone Trieste (Trieste, Italy) and at the BM8 beamline of ESRF (Grenoble, France). Spectra were acquired in transmission mode on samples cooled at 80 K with a liquid nitrogen cryostat. Ionization chambers were filled with Ar/N_2 mixtures at different pressure to achieve 20% absorption on I_0 and 60% on I_t. A double crystal Si (111) monochromator, with Pt-coated mirrors, was used to achieve a ΔE energy resolution around 1.4 eV. The data were collected with an energy step of 5 eV in the pre-edge region, 0.4 eV in the XANES region and with a constant k-step of 0.04 $Å^{-1}$ in the postedge region. Each sample was measured on a grid of nine spots ca. 1 mm apart to minimize beam exposure, with each scan lasting about 30 min, and all scans were averaged afterward. Data reduction was performed with Athena,[29] and the XANES spectra were simulated with FDMNES.[30]

3. RESULTS AND DISCUSSION

The formulas of the samples are summarized in Table 1. For the sake of simplicity, considering that all samples have TMSO as an organic cation and iodine as a halogen, all samples are labeled according to their bismuth percentage.

Table 1. Names and Stoichiometry of Samples Used in This Study

label	formula
Bi0	$(TMSO)PbI_3$
Bi8	$(TMSO)_3Pb_{2.67}Bi_{0.22}I_9$
Bi10	$(TMSO)_3Pb_{2.61}Bi_{0.26}I_9$
Bi22	$(TMSO)_3Pb_{2.13}Bi_{0.58}I_9$
Bi34	$(TMSO)_3Pb_{1.68}Bi_{0.88}I_9$
Bi58	$(TMSO)_3Pb_{0.99}Bi_{1.34}I_9$
Bi78	$(TMSO)_3Pb_{0.51}Bi_{1.66}I_9$
Bi100	$(TMSO)_3Bi_2I_9$

The structure of the $(TMSO)PbI_3$−$(TMSO)_3Bi_2I_9$ solid solutions has been recently described in detail.[10] Linear face-sharing chains of PbI_6/BiI_6 octahedra lie parallel to the ***a*** axis (see Figure 1), which therefore contracts and expands according to the relative occupation of metal sites with Pb, Bi, or metal vacancies, according to the defect chemical equation:

$$3Pb_{Pb}^{x} + 2BiI_3 \rightarrow 2Bi_{Pb}^{\bullet} + V_{Pb}^{''} + 3PbI_2 \quad (1)$$

In particular, the Pb/Bi/vacancy alternation is both nonperiodic and nonrandom, and it can be modeled to some extent as correlated disorder governed by a second-order stochastic matrix.[31]

For a $(TMSO)_8Pb_2Bi_4I_{24}$ composition, there are 16 possible dispositions of Pb/Bi/vacancy in the eight metal cation sites of a 2 × 1 × 1 supercell, labeled A to R (see Figure 1b). The configurational energy is then due to the different interaction terms between cation pairs (i.e., the next-nearest-neighbor Pb−Pb, Bi−Bi, Pb−Bi, etc. correlations), as summarized in Table 2.

The following structural models were used to compute the XANES spectra at the Pb and Bi L_3 edges: (1) isolated MI_6 octahedra (M = Pb or Bi); (2) 2 × 1 × 1 supercells with composition $(TMSO)_8Pb_2Bi_4I_{24}$, including all possible Pb/Bi arrangements in the eight metal cation sites, described in detail in ref 12. XANES spectra were then calculated for all configurations (Figure S1). For iodine, XANES spectra were simulated at the L_1-edge (Figure 2a): this absorption edge corresponds to the iodine 2s orbital, therefore probing dipole allowed transitions to 5p states, which are hybridized with metal 6s in the Pb/Bi−I bonds.[22] The simulated I L_1 spectra show substantial differences in the intensity of the white line and reflect the electronic density of states of the empty 5p orbitals of iodine. Compared to literature I L_1 spectra of 3D and 2D perovskites,[22] each octahedral face is shared here between two neighboring octahedra, and the local coordination of iodine atoms gives rise to a much different edge shape. The onset of the L_1 edge also correlates well with the position of the conduction band minimum. For instance, the energy of

https://doi.org/10.1021/acs.jpcc.3c03604
J. Phys. Chem. C 2023, 127, 18058−18066

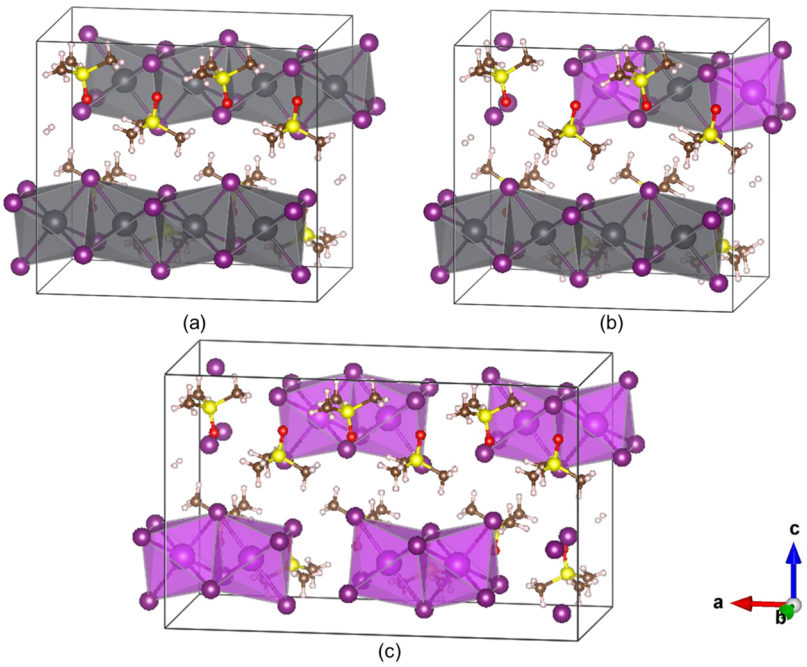

Figure 1. (a) Undoped $TMSO_8Pb_8I_{24}$ 2 × 1 × 1 supercell. (b) Doped $TMSO_8Pb_5Bi_2I_{24}$ supercell, configuration A. (c) $(TMSO)_3Bi_2I_9$ supercell. Iodine atoms are in violet, PbI_6 octahedra are in gray, BiI_6 octahedra in pink. Carbon, sulfur, oxygen, and hydrogen atoms are in gray, yellow, red, and white, respectively. The octahedral chains are aligned along the ***a*** direction.

Table 2. Energy of All Possible Configurations in $(TMSO)_8Pb_2Bi_4I_{24}$, Relative to Lowest-Energy Configuration "A"[a]

configuration	energy (eV)
A	0
B	0.58
C	0.58
D	0.56
E	0.48
F	0.52
G	1.11
H	1.04
I	0.97
L	1.03
M	1.48
N	1.39
O	1.39
P	1.47
Q	1.39
R	1.54

[a]Data taken from ref 12.

the I L_1 edge increases from configuration O to configurations A and B: the conduction band minimum also increases from configuration O to configurations A and B.[12] The absence of any pre-edge shoulder at low energy reflects the purely ionic interaction between $TMSO^+$ and iodide, with no mixing with the I p states.[12]

The experimental Pb and Bi L_3-edge spectra of the end members $TMSOPbI_3$ and $(TMSO)_3Bi_2I_9$ were compared with simulations from the respective crystal structures in Figure 1a,c (see Figure 3). For mixed samples, a first comparison (Figure 4) shows that all samples are very different from PbI_2 and BiI_3, and therefore, the decomposition to simple iodides from radiation damage can be reasonably excluded. All Pb near-edge

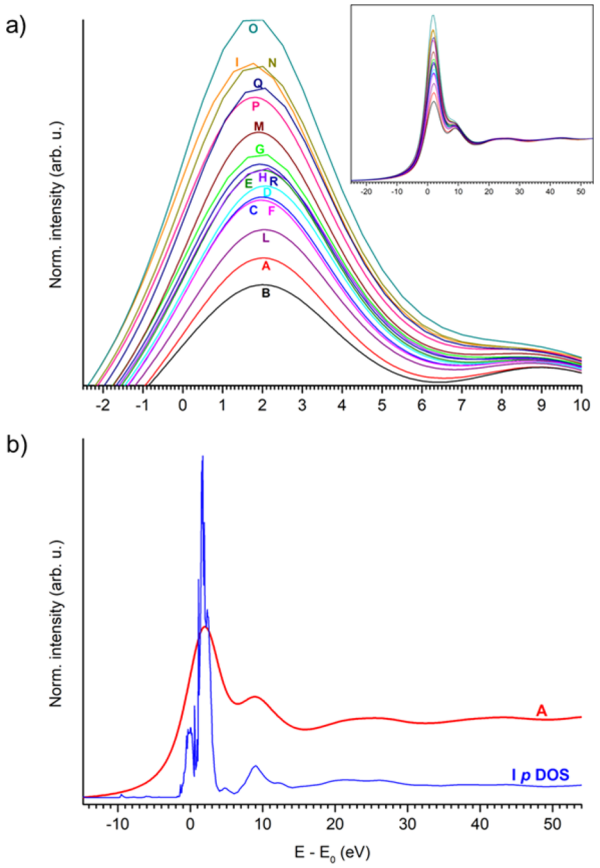

Figure 2. (a) XANES spectra of all configurations at the I L_1-edge; (b) I L_1-edge spectra (red) and the average of the p DOS (blue) of all iodine atoms.

features of samples look similar, while Bi shows varying intensities for the edge features (three peaks up to 25 eV after

https://doi.org/10.1021/acs.jpcc.3c03604
J. Phys. Chem. C 2023, 127, 18058−18066

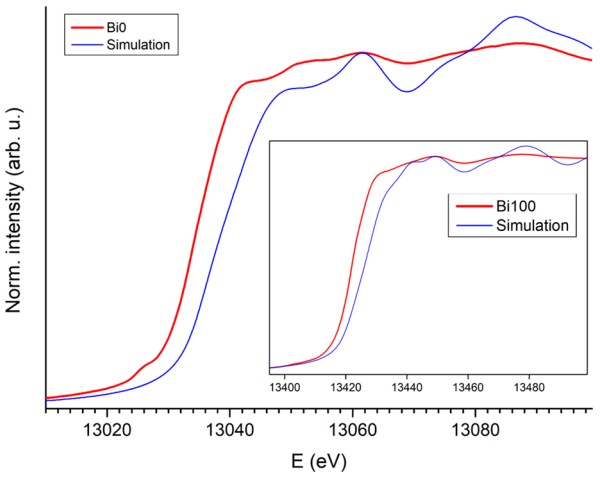

Figure 3. Pb L_3-edge experimental (red) and simulated (blue) XANES spectrum of $(TMSO)PbI_3$. Inset: Bi L_3-edge spectra experimental (red) and simulated (blue) XANES spectrum of $(TMSO)_3Bi_2I_9$.

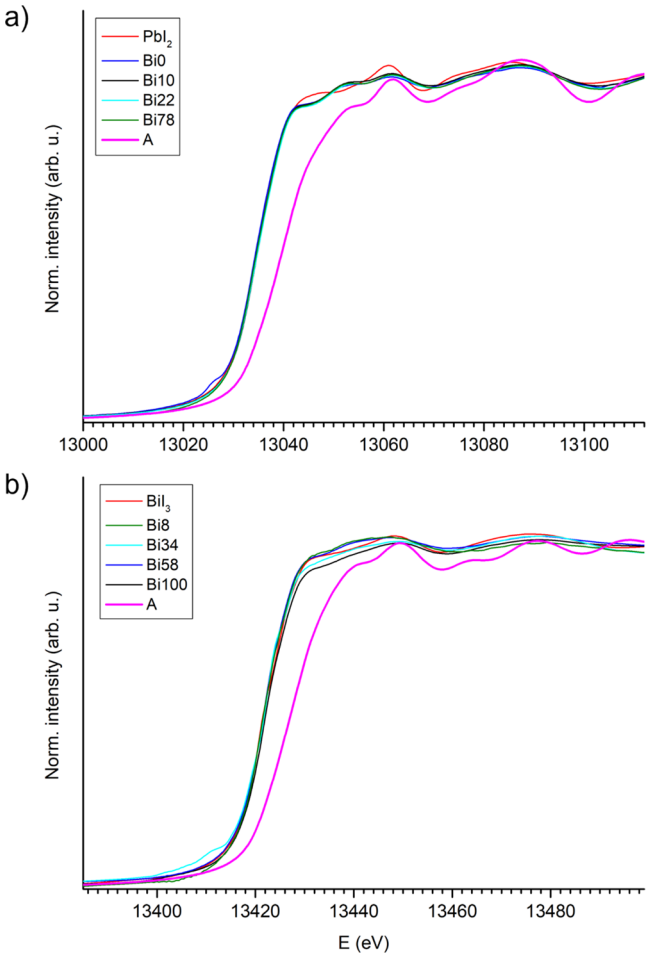

Figure 4. (a) Pb L_3-edge experimental XANES spectra compared to the precursor PbI_2, and the simulated spectrum of configuration A (thick line); (b) Bi L_3-edge experimental XANES spectra compared to the precursor BiI_3, and the simulated spectrum of configuration A (thick line).

the edge) depending on the Pb/Bi content. In general, configuration A is the one that resembles more the experimental data of all mixed samples for Pb and Bi L_3-edges, as seen especially in the position and intensity of maxima and minima >30 eV above the edge. This configuration features maximum segregation of Bi and vacancy defects in linear clusters [Bi−V−Bi], and having the lowest configurational energy it has the highest probability of being represented in an average ensemble in the bulk.

The different A-R configurations essentially differ for the weight of various metal−metal interoctahedral multiple scattering paths, while the nearest neighbor distances are the same in all of them. After assessing how different configurations affect the near-edge spectra, we now look into the role of each MI_6 octahedron. We extracted the octahedra of configuration A (five PbI_6 and two BiI_6, depicted in Figure 5a)

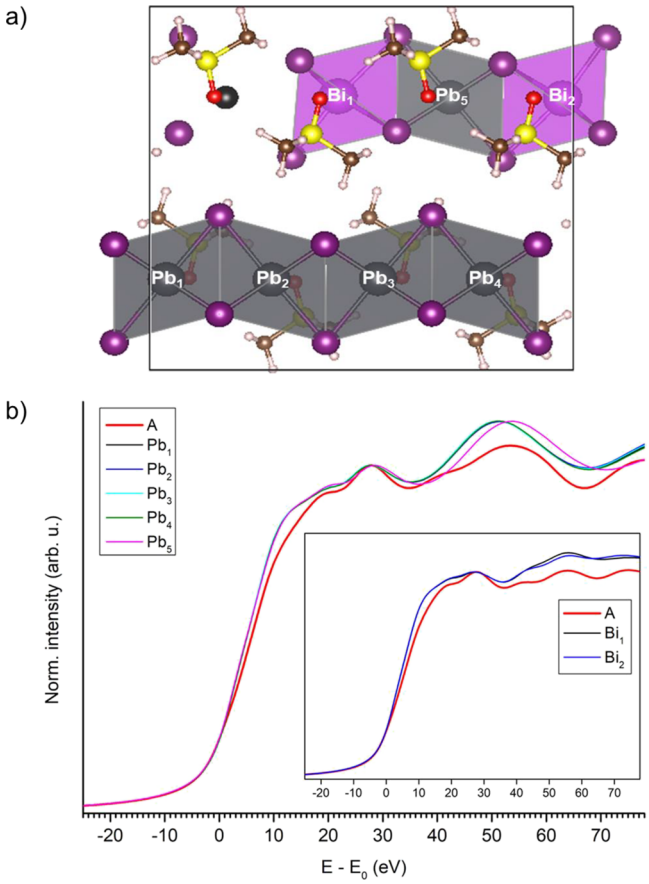

Figure 5. (a) Configuration A. Pb atoms are depicted in gray, Bi atoms in magenta, and vacancy in black. The color code for other atoms is the same as shown in Figure 1. (b) Simulated XANES spectra of configuration A compared with its individual component octahedra at the Pb L_3-edge (main panel) and Bi L_3-edge (inset).

to simulate their Pb and Bi XANES spectra (Figure 5b). With this approach, we can first evaluate whether an experimental XANES spectrum can be explained by the individual octahedra, or the whole configuration is needed. From inspection of Figure 5b, the essential features of the complete spectrum are still recognized in the spectrum of the isolated single octahedra, but important differences are evident in all portions of the spectrum, from the main edge to further peaks.

Comparing the experimental spectrum of mixed samples with the simulated spectra of configuration A and its octahedra (Figure 6), the individual octahedra (e.g., Pb_3 and Bi_2) are almost sufficient to explain all features of the experimental

https://doi.org/10.1021/acs.jpcc.3c03604
J. Phys. Chem. C 2023, 127, 18058−18066

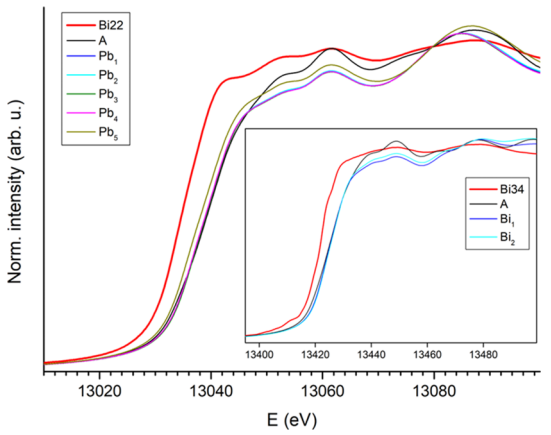

Figure 6. Experimental XANES spectra (thick red line) compared with the configuration A (black line) and individual octahedra (color lines) at the Pb L_3-edge (main plot) and Bi L_3-edge (inset).

spectra in the edge region. In particular, the main edge features are much better reproduced by a single octahedron than the complete structure involving M−I−M intraoctahedral paths, a surprising observation for a well-crystallized compound. This corroborates the general observation that the crystal structure is only a snapshot that does not fully capture the reality of a "wobbly" ensemble, and it is likely to underestimate both static and dynamic disorder.[15] This observation motivates the following investigation, based on the reduction of the structure to a sum of its octahedral units.

Simulations of the XANES spectra were then carried out on a series of distorted isolated PbI_6 and BiI_6 octahedra starting from pristine regular ones. The possible applied distortions were: (i) skewing of one iodine atom; (ii) isotropic compression and expansion; (iii) anisotropic elongation/compression along one axis; (iv) change of I−M−I bond angles. The effects of each modification on the Pb spectra are described in detail in the following: Bi spectra display mostly the same effects.

3.1. Iodine Skewing. Distortion of the octahedron by displacement along the *y* axis of an iodine atom, shown in the inset of Figure 7a, causes the reduction of the I−M−I angle by 6/7% ca. each step. From an angle of 90° in the pristine PbI_6 octahedron, an angle of 68.2° is obtained in *PbI_6_A_4* (inset of Figure 7a). To keep the volume of the octahedron constant, the Pb−I bond must elongate, resulting in a bond of 3.45 Å in *PbI_6_A_4* versus 3.2 Å in pristine PbI_6. This distortion does not cause consistent changes in the XAS spectra because there is the 7% elongation of a single bond Pb−I. As the distortion increases, there is a shift to left of the absolute maximum of 0.3 eV and the lows are shallower (Figure 7a).

3.2. Isotropic Compression. Reduction of the octahedron volume by about 2/3% at each step (inset of Figure 7b). From

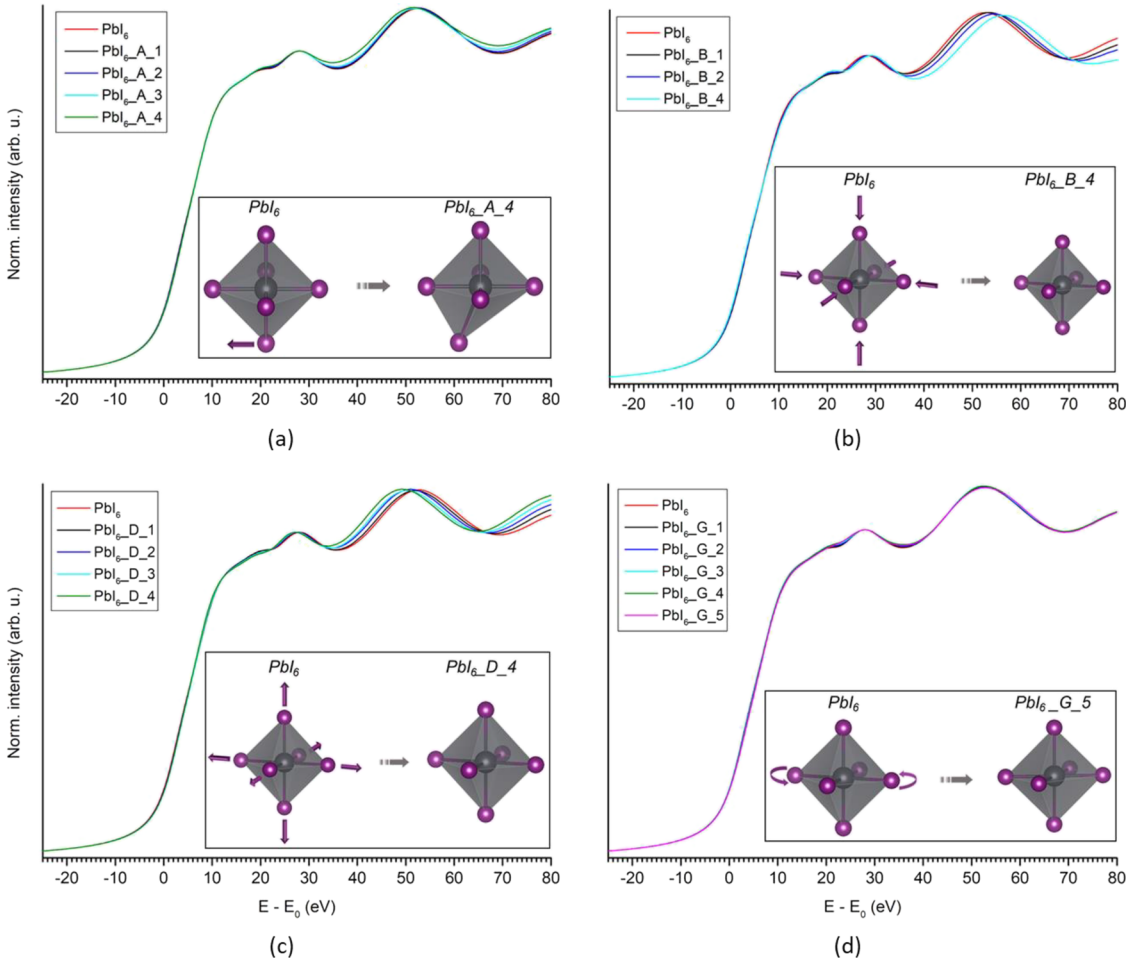

Figure 7. Simulated XANES spectra at the Pb L_3-edge of reference PbI_6 octahedron and different modes of octahedral distortion: (a) skewing; (b) isotropic compression; (c) isotropic expansion; (d) symmetric change of the equatorial I−Pb−I angle.

https://doi.org/10.1021/acs.jpcc.3c03604
J. Phys. Chem. C 2023, 127, 18058−18066

a volume of 43.7 Å^3, a volume of 39.72 Å^3 is obtained in *PbI$_6$_B_4*. The volume reduction causes in XAS spectra the shift to right of absolute maximum of ca. 1 eV each step and the lows are deeper (Figure 7b).

3.3. Axial Compression. Compression of the octahedron along the axial bonds causes the bond reduction of 0.05 Å each step. From a bond of 3.2 Å, a bond of 2.75 Å is obtained in *PbI$_6$_C_9* (inset of Figure 8a). In this case, the change in the two axial Pb−I bonds is important; this also causes a change in symmetry which leads to an evident change in the XAS spectra. As the reduction in axial bonds increases, there is a shift to the right of the absolute maximum, a reduction in intensity of the same peak, and an increase in the edge. In *PbI$_6$_C_9*, in which distortion is very important, the effects of multiple scattering can be seen (Figure 8a).

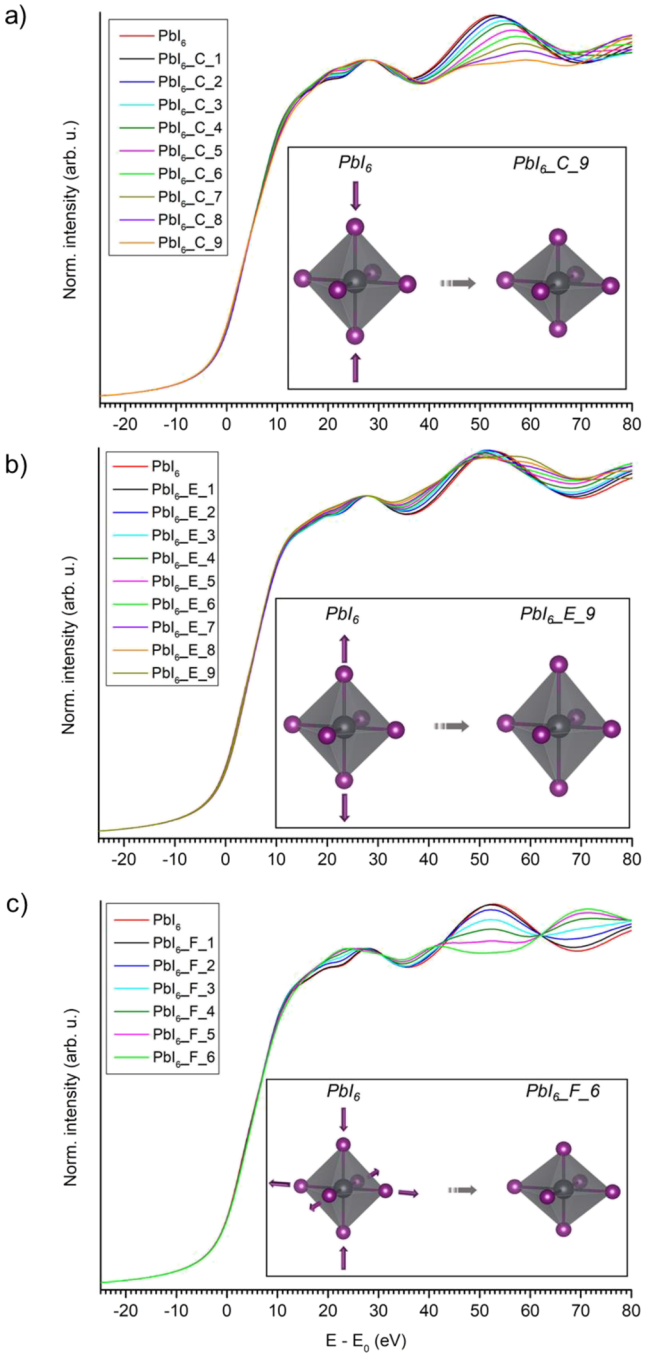

Figure 8. Simulated XANES spectra at the Pb L_3-edge of reference PbI_6 octahedron and further different modes of octahedral distortion: (a) axial compression; (b) axial elongation; (c) axial compression and equatorial elongation.

3.4. Isotropic Expansion. The increase of the octahedron volume is by about 2.3% at each step (inset of Figure 7c). From a volume of 43.7 Å^3, a volume of 47.92 Å^3 is obtained in *PbI$_6$_D_4*. The volume increase causes the maximum in the spectra to shift to the left by ca. 1 eV each step (Figure 7c). In this case, the minima are also systematically shallower.

3.5. Axial Elongation. Elongation of the octahedron along the axial bonds causes the bonds to increase by 0.05 Å each step. From a bond of 3.2 Å, a bond of 3.65 Å is obtained in *PbI$_6$_E_9* (inset of Figure 8b). In this case, the change in the two axial Pb−I bonds is not as important as in the case of compression, because the interaction of neighboring atoms becomes less important. As axial bonds increase, there are a slight shift to the left of the absolute maximum, a slight reduction in the intensity of the same peak, and an increase in the edge (Figure 8b).

3.6. Equatorial Elongation and Axial Compression. In this case, there is a compression of axial bonds and an elongation of equatorial bonds of 0.05 Å each step. From bonds of 3.2 Å, axial bonds of 2.9 Å and equatorial bonds of 3.5 Å are obtained in *PbI$_6$_F_6* (inset of Figure 8c). In this case, there is a strong impact on symmetry that greatly changes the XANES spectra (Figure 8c).

3.7. Rotation. The rotation of an equatorial bond axis causes the reduction of two angles and the increase of the other two by about 5° each step. From angles of 90°, two angles of 65° and two of 115° are obtained in *PbI$_6$_G_5* (inset of Figure 7d). In this case, there are no changes in the bond lengths, and therefore, this does not cause significant changes in the calculated spectra because multiple scattering effects are almost unaffected (Figure 7d).

The three modes of distortion depicted in Figure 8 have the biggest effects on the XANES spectra, and they all involve a reduction of symmetry from the O_h to D_{4h} point groups. On the contrary, the very large symmetry reduction obtained by skewing one iodine atom (Figure 7a) affects the XANES spectrum very little. It can be concluded that the spectrum is dominated by the presence and relative length of colinear I−M−I intra-octahedral paths.

For a deeper understanding of the effect of the metal-iodide distance on the XANES spectra, we analyzed the partial projection of the density of states at the absorber in all different PbI_6 octahedra. We then chose the simulated spectra that show substantial differences from pristine *PbI$_6$* pristine, i.e., *PbI$_6$_C_9*, *PbI$_6$_E_9*, and *PbI$_6$_F_6*, were compared with the respective calculated d DOS. In an undistorted PbI_6, the d_{z2} and d_{x2-y2} states are degenerate (Figure 9a): in octahedra with different axial/equatorial distances (Figure 9b−d) the geometrical distortion breaks the symmetry and also the degeneracy, causing the edge features to be blurred. The d_{x2-y2} DOS retains a strong sharp peak in the modes of distortion that involves axial compression (*PbI$_6$_C_9* and *PbI$_6$_F_6*), while in axial elongation (*PbI$_6$_C_9*, resembling a Jahn−Teller distortion) the two DOS of the two orbitals are only displaced, resulting in a flatter edge.

All the observations reported above suggest that the modifications on the absorption edges are eminently local in nature and they are mainly based on the relative length of colinear I−M−I intra-octahedral paths. This would allow to

https://doi.org/10.1021/acs.jpcc.3c03604
J. Phys. Chem. C 2023, 127, 18058−18066

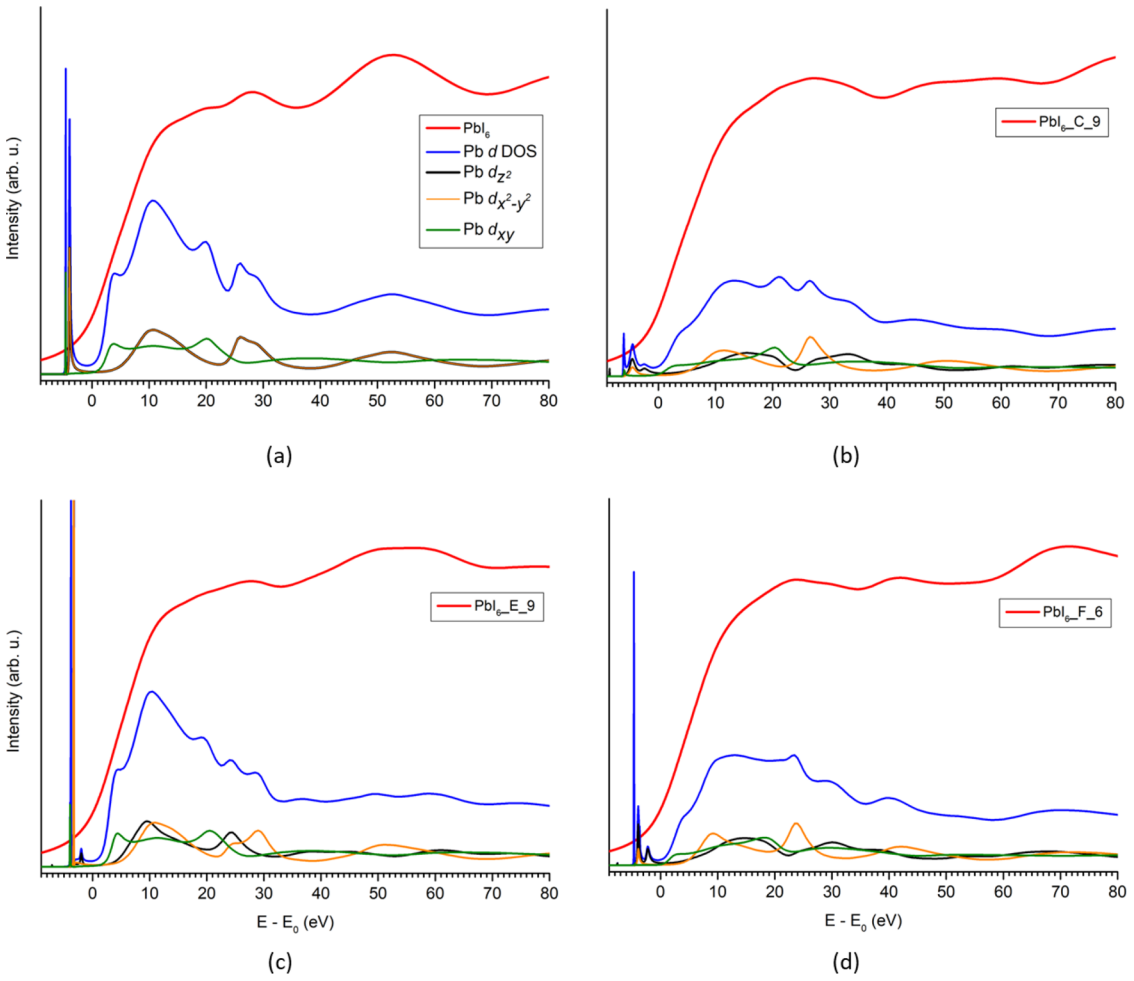

Figure 9. Simulated XANES spectra at the Pb L_3-edge and DOS of d orbitals: (a) reference PbI_6 octahedron; (b) axial compression; (c) axial elongation; (d) equatorial elongation and axial compression.

model the XANES or HERFD-XANES signals in terms of relatively simple modes of distortion during static or in situ/operando studies of halide perovskites. In this respect, many empirical attempts have been made recently to correlate XAFS spectra to synthetic parameters or post-synthetic treatments:[32,33] in fact, unsystematic choice of coordination shells and fitting parameters and large spread of the latter (Pb−I distances from 3.09 to 3.47 Å in a multiple-shell fit,[34] 3.13 Å in a single shell fit,[32] or even as low as 2.4−2.8 Å;[33] disorder factors from 0.006 to 0.019 $Å^2$) all hindered reliable structure−property relations for practical use of core spectroscopy methods to date. In general, EXAFS data of hybrid halide perovskites contain information on just one coordination shell.[32−34]

On the contrary, the near-edge portion of the spectrum is much less affected by static and dynamic disorder, and its sensitivity to symmetry and overall geometry (whether or not multiple scattering contributions play a role, as seen in this case) provide an idea complement to diffraction analysis.[35]

The understanding of structure−property relations is of pivotal importance for the future development of halide perovskites for solar cells with improved power conversion efficiency, one of the many fields of prospected application.

4. CONCLUSIONS

The evidence accumulated to date EXAFS data, vulnerable to the substantial static disorder typical of lead halide perovskites, has proven unconclusive to date, and eventually ineffectual to draw correlations with functional properties, or even other structural features. On the other hand, near-edge spectroscopy methods (XANES and HERFD-XANES) can provide interesting information on octahedral symmetry and cation arrangement in mixed-cation halide perovskites with various dimensionality, while requiring more rigorous ab initio simulations. Using a doped Pb/Bi monodimensional perovskite as a model compound, we show that the XANES spectra on several absorption edges are very sensitive to a number of subtle structural features of the metal-halide octahedral local geometry, while remaining independent of long-range multiple scattering effects that usually dominate the near-edge region. Connections to the electronic structures close to the Fermi energy can also be drawn case-by-case, as exemplified by the iodine L_1-edge. The extension of such an approach to other halide perovskites can be expected to provide simple structural correlations in the near future, usefully complementing other spectroscopic and diffraction techniques.[36]

https://doi.org/10.1021/acs.jpcc.3c03604
J. Phys. Chem. C 2023, 127, 18058−18066

■ ASSOCIATED CONTENT

Supporting Information

The Supporting Information is available free of charge at https://pubs.acs.org/doi/10.1021/acs.jpcc.3c03604.

Crystal structure and composition of all samples and simulated XANES spectra for all configurations and BiI_6 octahedra (PDF)

■ AUTHOR INFORMATION

Corresponding Author

Francesco Giannici − *Dipartimento di Fisica e Chimica "Emilio Segrè", Università di Palermo, Palermo I-90128, Italy;* orcid.org/0000-0003-3086-956X; Email: francesco.giannici@unipa.it

Authors

Simone Virga − *Dipartimento di Fisica e Chimica "Emilio Segrè", Università di Palermo, Palermo I-90128, Italy;* orcid.org/0000-0001-8022-5274

Alessandro Longo − *European Synchrotron Radiation Facility, Grenoble F-38043, France; Istituto per lo Studio dei Materiali Nanostrutturati ISMN-CNR, Palermo I-90146, Italy*

Candida Pipitone − *Dipartimento di Fisica e Chimica "Emilio Segrè", Università di Palermo, Palermo I-90128, Italy*

Complete contact information is available at: https://pubs.acs.org/10.1021/acs.jpcc.3c03604

Notes

The authors declare no competing financial interest.

■ ACKNOWLEDGMENTS

We acknowledge the European Synchrotron Radiation Facility for provision of beamtime on beamline BM8 (proposal MA-5455), and for access to the computing cluster, and the CERIC-ERIC consortium for providing access to the XAFS beamline at ELETTRA − Sincrotrone Trieste (proposal 20220258). We thank G. Das and A. Puri for assistance during the measurements.

■ REFERENCES

(1) Kojima, A.; Teshima, K.; Shirai, Y.; Miyasaka, T. Organometal Halide Perovskites as Visible-Light Sensitizers for Photovoltaic Cells. *J. Am. Chem. Soc.* **2009**, *131*, 6050−6051.

(2) Al-Ashouri, A.; Köhnen, E.; Li, B.; Magomedov, A.; Hempel, H.; Caprioglio, P.; Márquez, J. A.; Vilches, A. B. M.; Kasparavicius, E.; Smith, J. A.; et al. Monolithic perovskite/silicon tandem solar cell with >29% efficiency by enhanced hole extraction. *Science* **2020**, *370*, 1300−1309.

(3) Shi, Z.; Guo, J.; Chen, Y.; Li, Q.; Pan, Y.; Zhang, H.; Xia, Y.; Huang, W. Lead-Free Organic−Inorganic Hybrid Perovskites for Photovoltaic Applications: Recent Advances and Perspectives. *Adv. Mater.* **2017**, *29*, No. 1605005.

(4) Gollino, L.; Pauporté, T. Lead-Less Halide Perovskite Solar Cells. *Sol. RRL* **2021**, *5*, No. 2000616.

(5) Qiu, T.; Hu, Y.; Xu, F.; Yan, Z.; Bai, F.; Jia, G.; Zhang, S. Recent Advances in One-Dimensional Halide Perovskites for Optoelectronic Applications. *Nanoscale* **2018**, *10*, 20963−20989.

(6) Zhang, R.; Mao, X.; Cheng, P.; Yang, Y.; Yang, S.; Wumaier, T.; Deng, W.; Han, K. Bismuth Doped Lead-Free Two-Dimensional Tin Based Halide Perovskite Single Crystals. *J. Energy Chem.* **2019**, *36*, 1−6.

(7) Xiao, Z.; Song, Z.; Yan, Y. From Lead Halide Perovskites to Lead-Free Metal Halide Perovskites and Perovskite Derivatives. *Adv. Mater.* **2019**, *31*, No. 1803792.

(8) Xu, F.; Zhang, M.; Li, Z.; Yang, X.; Zhu, R. Challenges and Perspectives toward Future Wide-Bandgap Mixed-Halide Perovskite Photovoltaics. *Adv. Energy Mater.* **2023**, *13*, No. 2203911.

(9) Tong, Y.; Najar, A.; Wang, L.; Liu, L.; Du, M.; Yang, J.; Li, J.; Wang, K.; Liu, S. Wide-Bandgap Organic−Inorganic Lead Halide Perovskite Solar Cells. *Adv. Sci.* **2022**, *9*, No. 2105085.

(10) Pipitone, C.; Giannici, F.; Martorana, A.; García-Espejo, G.; Carlotto, S.; Casarin, M.; Guagliardi, A.; Masciocchi, N. Heterovalent Bi^{III}/Pb^{II} Ionic Substitution in One-Dimensional Trimethylsulfoxonium Halide Pseudo-Perovskites (X = I, Br). *J. Phys. Chem. C* **2021**, *125*, 11728−11742.

(11) Ursi, F.; Virga, S.; Pipitone, C.; Sanson, A.; Longo, A.; Giannici, F.; Martorana, A. Modelling the Structural Disorder in Trigonal-Prismatic Coordinated Transition Metal Dichalcogenides. *J. Appl. Crystallogr.* **2023**, *56*, 502−509.

(12) Pipitone, C.; Carlotto, S.; Casarin, M.; Longo, A.; Martorana, A.; Giannici, F. Bi^{3+} doping in 1D $((CH_3)_3SO)PbI_3$: a model for defect interactions in halide perovskites. *J. Mater. Chem. C* **2022**, *10*, 1458−1469.

(13) Zasimov, P.; Amidani, L.; Retegan, M.; Walter, O.; Caciuffo, R.; Kvashnina, K. O. HERFD-XANES and RIXS Study on the Electronic Structure of Trivalent Lanthanides across a Series of Isostructural Compounds. *Inorg. Chem.* **2022**, *61*, 1817−1830.

(14) Zhou, Y.; Doronkin, D. E.; Zhao, Z.; Plessow, P. N.; Jelic, J.; Detlefs, B.; Pruessmann, T.; Studt, F.; Grunwaldt, J. D. Photothermal Catalysis over Nonplasmonic Pt/TiO_2 Studied by Operando HERFD-XANES, Resonant XES, and DRIFTS. *ACS Catal.* **2018**, *8*, 11398−11406.

(15) Gorczyca, A.; Moizan, V.; Chizallet, C.; Proux, O.; Net, W. D.; Lahera, E.; Jean-Louis, H.; Raybaud, P.; Joly, Y. Monitoring Morphology and Hydrogen Coverage of Nanometric $PT/\gamma\text{-}Al_2O_3$ Particles by in Situ HERFD-XANES and Quantum Simulations. *Angew. Chem., Int. Ed.* **2014**, *53*, 12426−12429.

(16) Atkins, A. J.; Jacob, C. R.; Bauer, M. Probing the Electronic Structure of Substituted Ferrocenes with High-Resolution XANES Spectroscopy. *Chem. − Eur. J.* **2012**, *18*, 7021−7025.

(17) Proux, O.; Lahera, E.; Del Net, W.; Kieffer, I.; Rovezzi, M.; Testemale, D.; Irar, M.; Thomas, S.; Aguilar-Tapia, A.; Bazarkina, E. F.; et al. High-Energy Resolution Fluorescence Detected X-Ray Absorption Spectroscopy: A Powerful New Structural Tool in Environmental Biogeochemistry Sciences. *J. Environ. Qual.* **2017**, *46*, 1146−1157.

(18) Mei, B.; Liu, C.; Li, J.; Gu, S.; Du, X.; Lu, S.; Song, F.; Xu, W.; Jiang, Z. Operando HERFD-XANES and surface sensitive $\Delta\mu$ analyses identify the structural evolution of copper(II) phthalocyanine for electroreduction of CO_2. *J. Energy Chem.* **2022**, *64*, 1−7.

(19) Casals, E.; Barrena, R.; García, A.; González, E.; Delgado, L.; Busquets-Fité, M.; Font, X.; Arbiol, J.; Glatzel, P.; Kvashnina, K.; et al. Programmed Iron Oxide Nanoparticles Disintegration in Anaerobic Digesters Boosts Biogas Production. *Small* **2014**, *10*, 2801−2808.

(20) Zhu, X.; Su, H.; Marcus, R. A.; Michel-Beyerle, M. E. Computed and Experimental Absorption Spectra of the Perovskite $CH_3NH_3PbI_3$. *J. Phys. Chem. Lett.* **2014**, *5*, 3061−3065.

(21) Amat, A.; Mosconi, E.; Ronca, E.; Quarti, C.; Umari, P.; Nazeeruddin, M. K.; Grätzel, M.; De Angelis, F. Cation-Induced Band-Gap Tuning in Organohalide Perovskites: Interplay of Spin-Orbit Coupling and Octahedra Tilting. *Nano Lett.* **2014**, *14*, 3608−3616.

(22) Phuyal, D.; Safdari, M.; Pazoki, M.; Liu, P.; Philippe, B.; Kvashnina, K. O.; Karis, O.; Butorin, S. M.; Rensmo, H.; Edvinsson, T.; et al. Electronic Structure of Two-Dimensional Lead(II) Iodide Perovskites: An Experimental and Theoretical Study. *Chem. Mater.* **2018**, *30*, 4959−4967.

(23) Safdari, M.; Phuyal, D.; Philippe, B.; Svensson, P. H.; Butorin, S. M.; Kvashnina, K. O.; Rensmo, H.; Kloo, L.; Gardner, J. M. Impact of synthetic routes on the structural and physical properties of butyl-

1,4-diammonium lead iodide semiconductors. *J. Mater. Chem. A* **2017**, *5*, 11730−11738.
(24) Phuyal, D.; Jain, S. M.; Philippe, B.; Johansson, M. B.; Pazoki, M.; Kullgren, J.; Kvashnina, K. O.; Klintenberg, M.; Johansson, E. M. J.; Butorin, S. M.; et al. The electronic structure and band interface of cesium bismuth iodide on a titania heterostructure using hard X-ray spectroscopy. *J. Mater. Chem. A* **2018**, *6*, 9498−9505.
(25) Smith, M. A.; Chen, M.; Dai, Z.; Antolini, C.; Jayasekara, G. K.; Yadavalli, S. K.; Reinhart, B. J.; Padture, N. P.; Hayes, D. Real-Time Investigation of Sn(II) Oxidation in Pb-Free Halide Perovskites by X-Ray Absorption and Mössbauer Spectroscopy. *ACS Appl. Energy Mater.* **2021**, *4*, 4327−4332.
(26) Vorwerk, C.; Hartmann, C.; Cocchi, C.; Sadoughi, G.; Habisreutinger, S. N.; Félix, R.; Wilks, R. G.; Snaith, H. J.; Bär, M.; Draxl, C. Exciton-Dominated Core-Level Absorption Spectra of Hybrid Organic-Inorganic Lead Halide Perovskites. *J. Phys. Chem. Lett.* **2018**, *9*, 1852−1858.
(27) Drisdell, W. S.; Leppert, L.; Sutter-Fella, C. M.; Liang, Y.; Li, Y.; Ngo, Q. P.; Wan, L. F.; Gul, S.; Kroll, T.; Sokaras, D.; et al. Determining Atomic-Scale Structure and Composition of Organo-Lead Halide Perovskites by Combining High-Resolution X-Ray Absorption Spectroscopy and First-Principles Calculations. *ACS Energy Lett.* **2017**, *2*, 1183−1189.
(28) Toby, B. H.; Von Dreele, R. B. GSAS-II: the genesis of a modern open-source all purpose crystallography software package. *J. Appl. Crystallogr.* **2013**, *46*, 544−549.
(29) Ravel, B.; Newville, M. ATHENA, ARTEMIS, HEPHAESTUS: data analysis for X-ray absorption spectroscopy using IFEFFIT. *J. Synchrotron Radiat.* **2005**, *12*, 537−541.
(30) Bunău, O.; Joly, Y. Self-consistent sspects of x-ray absorption calculations. *J. Phys.: Condens. Matter* **2009**, *21*, No. 345501.
(31) Pipitone, C.; Ursi, F.; Giannici, F.; Longo, A.; Guagliardi, A.; Masciocchi, N.; Martorana, A. Modeling bismuth insertion in 1D hybrid lead halide $TMSO(Pb_xBi_y)I_3$ Pseudo-Perovskites. *Nanotechnology* **2022**, *33*, 425703.
(32) Kang, D. H.; Park, Y. J.; Jeon, Y. S.; Park, N. G. Extended X-Ray Absorption Fine Structure (EXAFS) of $FAPbI_3$ for Understanding Local Structure-Stability Relation in Perovskite Solar Cells. *J. Energy Chem.* **2022**, *67*, 549−554.
(33) Liu, B.; Cui, R.; Huang, H.; Guo, X.; Dong, J.; Yao, H.; Li, Y.; Zhao, D.; Wang, J.; Zhang, J.; et al. Elucidating the Mechanisms Underlying PCBM Enhancement of $CH_3NH_3PbI_3$ Perovskite Solar Cells Using GIXRD and XAFS. *J. Mater. Chem. A* **2020**, *8*, 3145−3153.
(34) Nandi, P.; Mahana, S.; Welter, E.; Topwal, D. Probing the Role of Local Structure in Driving the Stability of Halide Perovskites $CH_3NH_3PbX_3$. *J. Phys. Chem. C* **2021**, *125*, 24655−24662.
(35) Morana, M.; Wiktor, J.; Coduri, M.; Chiara, R.; Giacobbe, C.; Bright, E. L.; Ambrosio, F.; De Angelis, F.; Malavasi, L. Cubic or Not Cubic? Combined Experimental and Computational Investigation of the Short-Range Order of Tin Halide Perovskites. *J. Phys. Chem. Lett.* **2023**, *14*, 2178−2186.
(36) Cannelli, O.; Wiktor, J.; Colonna, N.; Leroy, L.; Puppin, M.; Bacellar, C.; Sadykov, I.; Krieg, F.; Smolentsev, G.; Kovalenko, M. V.; et al. Atomic-Level Description of Thermal Fluctuations in Inorganic Lead Halide Perovskites. *J. Phys. Chem. Lett.* **2022**, *13*, 3382−3391.

https://doi.org/10.1021/acs.jpcc.3c03604
J. Phys. Chem. C 2023, 127, 18058−18066